Flow, Turbulence and Combustion (2023) 110:969–991
https://doi.org/10.1007/s10494-023-00407-4

RESEARCH

Turbulent Drag Reduction by Travelling Waves of Spanwise Lorentz Force

Qiang Yang[1,2] · **Yongmann M. Chung**[1]

Received: 26 September 2022 / Accepted: 24 February 2023 / Published online: 7 April 2023

Abstract
Travelling waves induced by spanwise Lorentz force for skin-friction drag reduction are studied in the present work using direct numerical simulations, with particular focus on the streamwise and spanwise travelling waves. The overall picture of drag reduction in the frequency-wavenumber parameter space, $\omega - \kappa_x - \kappa_z$ is uncovered. It is found that both drag reduction maps for the streamwise and spanwise travelling waves are featured with a drag reduction ($\mathcal{DR}$) region and a drag increase ($\mathcal{DI}$) region. For the streamwise travelling wave of spanwise Lorentz force, the $\mathcal{DR}$ and $\mathcal{DI}$ regions are located in the same parameter regime compared to that of the streamwise travelling wave of spanwise wall velocity, while for the spanwise travelling wave, the $\mathcal{DR}$ variation at any fixed κ_z is similar to that of spanwise oscillating Lorentz force. An exploration of the oblique travelling wave with an angle to the mean flow shows that the optimal drag reduction appears when the wave travels backward relative to the flow direction, and the "ribbon" structure is a general phenomenon appearing in all oblique travelling wave cases. The ensemble averaged positive and negative quasi-streamwise vortices become asymmetric when the travelling wave is imposed, and the near-wall high- and low-speed streaks are significantly tilted in the spanwise direction. Spanwise oscillation, streamwise and spanwise travelling waves share strong similarity in the statistics, energy spectra as well as turbulent structure modulation.

Keywords Drag reduction · Flow control · Lorentz force · Turbulence simulation

1 Introduction

Turbulent skin-friction drag reduction control has huge environmental and economic impacts on the global transportation (Leschziner et al. 2011), thus many studies have been conducted to achieve drag reduction (Karniadakis and Choi 2003; Quadrio 2011; Corke and Thomas 2018; Leschziner 2020; Ricco et al. 2021). One attractive control method for ocean applications is to use surface based electric-magnetic actuators, which generate

✉ Yongmann M. Chung
Y.M.Chung@warwick.ac.uk

[1] School of Engineering, University of Warwick, Coventry CV4 7AL, UK

[2] Present Address: State Key Laboratory of Aerodynamics, China Aerodynamics Research and Development Centre, Mianyang 621000, People's Republic of China

Lorentz body force in the near-wall region to modulate the turbulent structures (Du and Karniadakis 2000), as the near-wall streaks and quasi-streamwise vortices form a self-sustaining cycle and contribute significantly to the turbulent skin friction (Hamilton et al. 1995; Kravchenko et al. 1993; de Giovanetti et al. 2016; Yang et al. 2019). The electric-magnetic actuators provide us the freedom to bring novel near-wall drag reduction control ideas into practice. For instance, Henoch and Stace (1995); Crawford and Karniadakis (1997) studied the streamwise Lorentz force for drag reduction, but both studies showed a pumping effect resulting in drag increase. Berger et al. (2000) used the near-wall Lorentz force for the closed-loop opposition control (Choi and Moin 1994), and achieved 40% drag reduction at $Re_\tau = 100$. Instead, Mamori and Fukagata (2014) studied the wave-like near-wall Lorentz force for the opposition control, and also found 40% drag reduction. The drag reduction by Lorentz force has been subsequently confirmed in a series of experiments as well (e.g. Du et al. 2002; Breuer et al. 2004; Pang and Choi 2004).

One effective way of drag reduction by electric-magnetic actuators is to generate spanwise Lorentz force with respect to the flow direction (Berger et al. 2000; Du et al. 2002; Huang et al. 2010), which was inspired by the spanwise wall oscillation (Jung et al. 1992). In the spanwise oscillating Lorentz force case, the force is exponentially decayed in the wall-normal direction, and sinusoidally modulated in time as below,

$$f = Ae^{-y/\Delta} \sin\left(\frac{2\pi}{T}t\right) = Ae^{-y/\Delta} \sin\left(\omega t\right), \tag{1}$$

where A is the force strength, Δ the force penetration depth, and T (or ω) the oscillation period (or angular frequency). With this strategy, Berger et al. (2000) obtained 40% drag reduction at $Re_\tau = 200$, which is comparable to the spanwise wall oscillation case (Jung et al. 1992). The optimal oscillation period was found to be within the range of $T^+_{opt} = 25 \sim 125$ (here the superscript + indicates non-dimensionalised in the viscous units). Berger et al. (2000) showed that the spanwise Lorentz force generates a similar spanwise mean velocity profile compared to the Stokes layer in the spanwise wall oscillation case, and we term it as the Lorentz force generated Stokes layer (LGSL) in the present study. The drag reduction by spanwise oscillating Lorentz force was also numerically verified in boundary layer flow by Lee and Sung (2005), with 20% drag reduction achieved. Recently, Zhao et al. (2019) applied circular Lorentz force on the cylinder boundary layer, and achieved 42.6% drag reduction. To avoid alternating the polarity of the actuator for the spanwise oscillating Lorentz force, Berger et al. (2000) further proposed the spatially oscillating Lorentz force configuration, i.e. the streamwise stationary waveform, shown as below,

$$f = Ae^{-y/\Delta} \sin\left(\frac{2\pi}{\lambda_x}x\right) = Ae^{-y/\Delta} \sin\left(\kappa_x x\right), \tag{2}$$

where λ_x (or κ_x) is the streamwise wavelength (or wavenumber). A similar amount of drag reduction of 30% was obtained compared to the spanwise oscillating Lorentz force. The optimal streamwise wavelength ($\lambda^+_{x,opt} = 250 \sim 1250$) for the streamwise stationary wave case was found to correlate with the optimal oscillation period ($T^+_{opt} = 25 \sim 125$) for the spanwise oscillation case by a convection velocity, i.e. $\mathscr{U}^+_c = 10$. This observation is similar to the streamwise stationary wave of spanwise wall velocity (Viotti et al. 2009), which has been studied extensively in laboratory (Quadrio et al. 2009; Auteri et al. 2010; Hurst et al. 2014; Bird et al. 2018; Albers et al. 2020; Marusic et al. 2021).

A more general travelling wave form is given by Huang et al. (2014) as below,

$$f = Ae^{-y/\Delta}\sin\left(\frac{2\pi}{\lambda_x}x + \frac{2\pi}{\lambda_z}z - \frac{2\pi}{T}t\right) = Ae^{-y/\Delta}\sin\left(\kappa_x x + \kappa_z z - \omega t\right), \tag{3}$$

where λ_z (or κ_z) is the spanwise wavelength (or wavenumber). Equation 3 represents a two-dimensional plane wave, with the wave angle to the mean flow direction $\theta = \tan^{-1}(\kappa_z/\kappa_x)$, the wavenumber $\kappa = \sqrt{\kappa_x^2 + \kappa_z^2}$, and the wave speed $c = \omega/\kappa$. When $(\kappa_x, \kappa_z) = (0, 0)$, it corresponds to the spanwise oscillating Lorentz force; when $\kappa_x = 0$, it corresponds to the spanwise travelling wave; and when $\kappa_z = 0$, it corresponds to the streamwise travelling wave. Drag reduction by different waveforms has been studied extensively during the past decades (Berger et al. 2000; Du et al. 2002; Huang et al. 2010; Xie and Quadrio 2013; Huang et al. 2014; Jiang et al. 2019), and a summary of the control parameters investigated in these studies is listed in Table 1.

The spanwise travelling wave of spanwise Lorentz force was first studied by Du et al. (2002), who obtained more than 30% drag reduction, similar to the spanwise oscillating Lorentz force, with higher drag reduction appearing at longer spanwise wavelengths. One particular observation by Du et al. (2002) is the wide "ribbon" structure in the spanwise travelling wave case, within which the near-wall streaks become invisible. However, the "ribbon" structure does neither exist in the spanwise oscillating Lorentz force case, nor in other near-wall drag reduction controls, such as the riblets and the spanwise wall oscillation. The authors argued that under the spanwise travelling wave of Lorentz force, it is the "ribbon" structure enhanced streamwise vortices that causes the weakening of the streak intensity, and that is the fundamental difference between the spanwise travelling wave and the spanwise oscillating Lorentz force. This observation was further supported by Huang et al. (2011) with their direct numerical simulation (DNS) data. The spanwise travelling Lorentz force was further explored by Xie and Quadrio (2013) in a four-dimensional parameter space, i.e. $\omega^+ - \kappa_z^+ - A - \Delta^+$ at $Re_\tau = 200$, and they concluded that the drag reduction by spanwise travelling wave of spanwise Lorentz force is always underperformed compared to that of spanwise oscillating Lorentz force. Meanwhile, the streamwise travelling wave of spanwise Lorentz force was investigated by Huang et al. (2010). The authors conducted several DNS simulations at the optimal oscillation period $T_{opt}^+ = 100$ to understand the effect of the streamwise wavenumber κ_x^+. The maximum drag reduction, slightly higher than that of the spanwise oscillating Lorentz force case, was found at $\lambda_x^+ = 188$. Recently, Huang et al. (2014) explored the drag reduction map for oblique travelling waves in a two-dimensional wavenumber space $\kappa_x^+ - \kappa_z^+$, and found that the maximum drag reduction appears when the wave travels in the streamwise direction.

Table 1 Parameters for drag reduction by spanwise Lorentz force studied in literature

Previous studies	Re_τ	Waveform	A	Δ^+	T^+	λ_x^+	λ_z^+
Berger et al. (2000)	200	$\sin(\omega t)\sin(\kappa_x x)$	0.13 ∼ 1.5	5 ∼ 20	25 ∼ 500	300 ∼ 2400	–
Du et al. (2002)	150	$\sin(\omega t)$ $\sin(\kappa_z z - \omega t)$	1.3 ∼ 20	0.5 ∼ 3	25 ∼ 200	–	210 ∼ 840
Huang et al. (2010)	180	$\sin(\kappa_x x - \omega t)$	2.3	3.6	100	60 ∼ 1130	–
Xie and Quadrio (2013)	200	$\sin(\kappa_z z - \omega t)$	0.1 ∼ 4.5	20	5 ∼ 100	–	125 ∼
Huang et al. (2014)	180	$\sin(\kappa_x x + \kappa_z z - \omega t)$	1.2	3.6	120	50 ∼ 750	50 ∼ 750

Even though there have been many studies concerning various travelling waves of spanwise Lorentz force, three main issues still need to be addressed. Firstly, regarding the travelling wave angle effect, only very limited cases are available in the discrete (κ_x^+, κ_z^+) space, and the dynamic variation of the flow with the travelling wave angle remains unclear, which needs more thorough investigation, especially with better design of the numerical experiments for channel flow. Secondly, among the above studies, majority of the work focused on the parameter study in a small potion of the $(A, \Delta^+, \omega^+, \kappa_x^+, \kappa_z^+)$ space, and the explored parameter space is not wide enough to give an overall picture of the drag reduction due to spanwise Lorentz force, i.e. the $\mathcal{DR}$ and $\mathcal{DI}$ regions. Thirdly, the drag reduction mechanism for the spanwise oscillation and the travelling waves of Lorentz force is not conclusive yet, especially the similarity of the control effect under all these different travelling waves is still missing (for instance, Du et al. 2002). The aim of the present study is to perform a systematic study of drag reduction by travelling waves of spanwise Lorentz force, thus improve the understanding of fundamental turbulent structure modulation through intensive statistical and dynamical analyses, and highlight the similarity in the drag reduction mechanism shared by the spanwise oscillating Lorentz force, the streamwise, spanwise and oblique travelling waves.

The paper is organised as following: the simulation setup is given in Sect. 2, followed by the main results, including drag reduction maps, energy spectra analysis and structure dynamics in Sect. 3, and it is finally concluded in Sect. 4.

2 Simulation Setup

The incompressible Navier–Stokes equations with the body force term f_i are shown as,

$$\begin{aligned} \frac{\partial u_i}{\partial t} + u_j \frac{\partial u_i}{\partial x_j} &= -\frac{\partial p}{\partial x_i} + \frac{1}{Re} \frac{\partial^2 u_i}{\partial x_j^2} + f_i, \\ \frac{\partial u_i}{\partial x_i} &= 0, \end{aligned} \tag{4}$$

where the subscript $(i, j = 1, 2, 3)$ represents the x, y and z direction, respectively. x_i, u_i and f_i represent the coordinate, the velocity and the body force in the corresponding direction. The Reynolds number is based on the bulk mean velocity of the channel U_m and the half channel height h, i.e. $Re = U_m h/\nu = 3150$ in the present study, where ν is the dynamic viscosity; the corresponding friction Reynolds number is $Re_\tau = u_\tau h/\nu = 200$, where $u_\tau (\equiv \sqrt{\tau_w/\rho})$ is the friction velocity, with τ_w the streamwise wall shear stress and ρ the fluid density. All variables are non-dimensionalised by the corresonding outer units by default, i.e. the half channel height h and the bulk mean velocity U_m, e.g. the body force is non-dimensionalised by U_m^2/h. Those variables scaled in the viscous units of the no-control case and the controlled case are indicated by the superscript $^+$ and , respectively. The equations are solved using an in-house second-order fully implicit finite volume code. The time advancement uses a frictional step method with the Crank-Nicolson scheme, and all the spatial terms are discretised using the second-order central difference. Taking advantage of the periodic boundary conditions in the two wall-parallel directions, the Poisson equation is solved in the Fourier space with a tridiagonal matrix inversion in the wall-normal direction. The in-house code has been verified extensively in our previous studies (see Chung and Talha 2011; Hurst et al. 2014; Talha and Chung 2015).

Table 2 Main parameters for typical Lorentz force controlled cases at $A = 0.5$, $\Delta^+ = 10$

Case	$L_x \times L_z$	$\Delta x^+ \times \Delta z^+$	ω^+	κ_x^+	κ_z^+	θ	$\mathcal{DR}$	Line style
OC	16×6	5×2.5	0.06	0	0	–	27.8	—
FST	16×6	5×2.5	0.06	0.002	0	0°	10.8	-.-.-
SP	16×12	5×2.5	0.06	0	0.0026	90°	25.7	- - -
BST	16×6	5×2.5	−0.06	0.002	0	180°	31.4	.
OB	16×16	2.5×2.5	±0.06	0.002\0.0	0.0\0.002	–	–	-

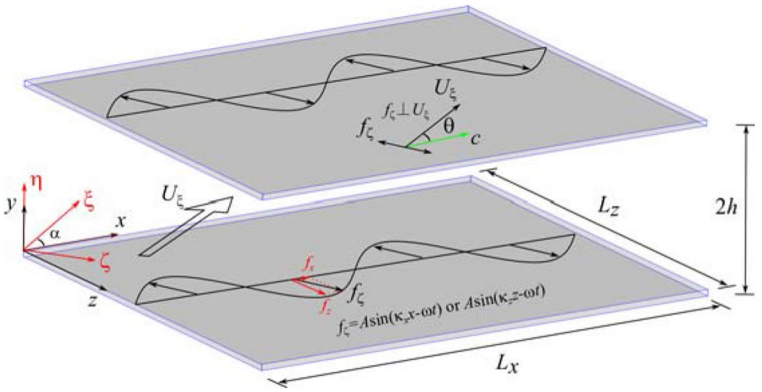

Fig. 1 Schematic of skin-friction drag control by travelling waves of spanwise Lorentz force. The streamwise mean flow U_ξ has an angle of θ to the wave travelling direction (indicated by the green arrow). (ξ, η, ζ) is the transformed coordinate, with ξ, η and ζ indicating the streamwise, wall-normal and spanwise direction of the flow. For streamwise and spanwise travelling wave configurations, the transformed coordinate (ξ, η, ζ) is identical to the original one (x, y, z), i.e. $\alpha = 0°$. f_x and f_z are the two components of the generated Lorentz force f_ζ onto the x and z directions

The Lorentz force shown in equation 3 is applied in the spanwise direction, which presents exponential decay in the wall-normal direction and sinusoidal variation in space and time. Here, the main interest is to investigate three different types of travelling waves, i.e. the forward streamwise travelling wave ($\theta = 0°$, $\kappa_z^+ = 0$, $\omega^+ > 0$), the spanwise travelling wave ($\theta = 90°$, $\kappa_x^+ = 0$), and the backward streamwise travelling wave ($\theta = 180°$, $\kappa_z^+ = 0$, $\omega^+ < 0$), as illustrated in Fig. 1. The main analysis focus on four typical cases for each configuration: OC for the spanwise oscillation case at $\omega^+ = 0.06$, FST for the forward streamwise travelling wave case at $(\omega^+, \kappa_x^+) = (0.06, 0.002)$, SP for the spanwise travelling wave case at $(\omega^+, \kappa_z^+) = (0.06, 0.0026)$, and BST for the backward streamwise travelling wave case at $(\omega^+, \kappa_x^+) = (-0.06, 0.002)$. The control parameters are listed in Table 2.

For the oblique travelling wave angle study, in order to vary the wave angle θ at a fixed wavenumber κ^+, the wave travelling direction is chosen to align in either x or z direction, whereas the mean flow direction varies gradually, as shown in Fig. 1. The domain size and grid resolution are set to be identical in the x and z directions to make them completely equivalent (see OB in Table 2). Four no-control cases, which have the angle $\alpha = 0°, 15°, 30°$ and 45° with respect to the x direction, have been first performed as the base flows. For each base flow, the travelling wave is then applied in the positive x, negative x, positive

z or negative z direction, which corresponds to the travelling wave angle of α, $180° - \alpha$, $90° - \alpha$ and $90° + \alpha$, respectively. In such a way, the angle effect can be studied for a fixed wavelength in the range of $\theta = 0° \sim 180°$ with an interval of 15° (13 cases in total). To seek the potential maximum drag reduction, the wavenumber is chosen to be $\kappa^+ = 0.002$ and the oscillation frequency $\omega^+ = \pm 0.06$, such that at $(\kappa_x^+, \kappa_z^+, \omega^+, \theta) = (0.002, 0, -0.06, 180°)$ it corresponds to the optimal streamwise travelling wave case, i.e. BST. When $\theta = 0°$, the oblique travelling wave case recovers FST; when $\theta = 90°$, it matches SP, but the wavenumber is slightly smaller due to the restriction in the spanwise domain size (see Table 2 for comparison).

The spanwise Lorentz force is applied in the near-wall regions of the top and bottom walls of the channel, with the force varying in the same phase. The grid resolution of $\Delta x^+ = 5$, $\Delta y^+_{min} = 0.4$, $\Delta y^+_{max} = 6$ and $\Delta z^+ = 2.5$ are used in the x, y and z direction, respectively, which shows a good agreement with the literature data for plane Poiseuille flow as tested by Hurst et al. (2014). The box sizes for the travelling wave cases are shown in Table 2. For the spanwise travelling wave study, the spanwise domain is doubled in order to explore larger spanwise wavelengths. The time step is fixed at $\Delta t^+ = 0.2$. The streamwise mass flow rate is kept constant during the Lorentz force control by dynamically adjusting the streamwise mean pressure gradient based on the skin friction. The simulations are typically run for a long period of $t^+ = 10000$, with the first $t^+ = 4000$ statistics discarded to remove the initial transient effect. The drag reduction is then evaluated through time and space averaged skin friction, i.e. $\mathcal{DR}(\%) = (C_{f,0} - C_f)/C_{f,0}$, where C_f and $C_{f,0}$ are the skin-friction coefficients of the no-control and controlled cases, respectively. The turbulent statistics are sampled by using the triple decomposition, i.e. $u = U + \tilde{u} + u'$, where U is the time and space averaged mean component, i.e. $U = \langle u \rangle_{x,z,t}$, $\tilde{u}$ is the phase mean component with U removed, and u' is the turbulent stochastic fluctuation. Grid resolution, domain size and time step are tested for the spanwise oscillating Lorentz force case OC, and the results are shown in Table 3 with the standard uncertainty $\delta(\cdot)$ given in the brackets. For the uncertainty evaluation in $\mathcal{DR}$, we adopt the propagating formula as below by following Gatti and Quadrio (2016),

$$\delta\mathcal{DR}(\%) = \frac{C_f}{C_{f,0}} \sqrt{\left(\frac{\delta C_f}{C_f}\right)^2 + \left(\frac{\delta C_{f,0}}{C_{f,0}}\right)^2}. \tag{5}$$

Table 3 Grid resolution and domain size test for the spanwise oscillating Lorentz force case (OC)

Case	$L_x \times L_z$	$\Delta x^+ \times \Delta z^+$	Δt^+	$C_f\,(\delta C_f) \times 10^3$	$\mathcal{DR}\,(\delta\mathcal{DR})$
C1	16×6	5×2.5	0.2	7.72 (±0.08)	27.8 (±1.5)
C2	16×6	10×2.5	0.2	5.59 (±0.11)	27.6 (±1.6)
C3	16×6	2.5×2.5	0.2	5.68 (±0.12)	26.4 (±1.9)
C4	16×6	5×5	0.2	5.60 (±0.10)	27.4 (±1.5)
C5	16×6	5×1.25	0.2	5.63 (±0.11)	27.1 (±1.6)
C6	32×6	5×2.5	0.2	5.67 (±0.08)	26.6 (±1.3)
C7	16×12	5×2.5	0.2	5.61 (±0.10)	27.3 (±1.5)
C8	16×6	5×2.5	0.1	5.64 (±0.14)	26.9 (±2.0)

The skin-friction coefficient for the no-control case is $C_{f,0} = 7.72 \times 10^{-3}$ with the standard uncertainty $\delta C_{f,0} = \pm 0.08 \times 10^{-3}$

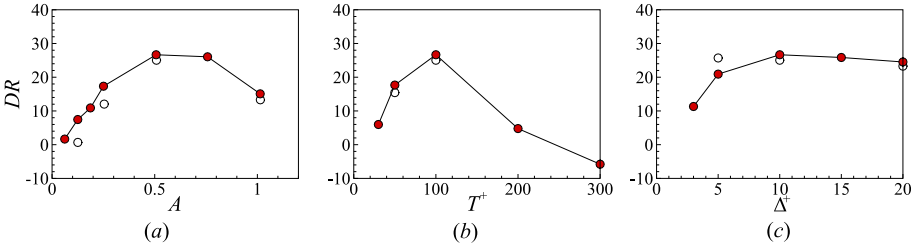

Fig. 2 Effect on drag reduction $\mathcal{DR}$ for OC from **a** Lorentz force strength A, **b** oscillation period T^+, and **c** Lorentz force penetration depth Δ^+. The Lorentz force parameter of the baseline case is $(A, T^+, \Delta^+) = (0.5, 100, 10)$. Close symbols are the present data, and open symbols are from Berger et al. (2000)

As the no-control channel flow at $Re_\tau \approx 200$ is a standard benchmark case, which we have done a thorough independence test in our previous study (e.g. Hurst et al. 2014), here we use the $C_{f,0}$ value of C1 as the reference for all the controlled cases to compute the $\mathcal{DR}$ values. For all the test cases, the maximum relative change in $\mathcal{DR}$ is around 5%, which appears in the streamwise resolution variation, then followed by the streamwise domain and time step change; while the relative $\mathcal{DR}$ change is much smaller ($< 3\%$) for the spanwise resolution and spanwise domain size variations.

The spanwise oscillation cases are first studied to validate the methodology used in the present study with the comparison at $Re_\tau = 200$ to Berger et al. (2000), as shown in Fig. 2. The baseline case is chosen at $(A, T^+, \Delta^+) = (0.5, 100, 10)$ according to the parameter study by Berger et al. (2000), and the Lorentz force parameters are then varied to test the effect on the drag reduction. A good comparison is observed, except the region where the Lorentz force strength A is small, or the Lorentz force penetration depth Δ^+ is small, but the trend prediction agrees well with each other. It is noted that a much smaller domain size, i.e. $(L_x, L_z) = (2\pi, 4\pi/3)$ was employed by Berger et al. (2000). According to the domain size test result in Table 3, this can bring high uncertainty in the $\mathcal{DR}$ value evaluation. Based on the observation, there is an optimal value for each control parameter of (A, T^+, Δ^+) when the other two are fixed, and the chosen baseline with $(A, T^+, \Delta^+) = (0.5, 100, 10)$ is the local maxima.

3 Results

3.1 Oblique Travelling Waves

Instantaneous snapshots for the velocity magnitude close to the wall at $y^+ \approx 5$ are shown in Fig. 3 for oblique travelling wave cases at $A = 0.5$, $\Delta^+ = 10$, $\kappa^+ = 0.002$ and $\omega^+ = 0.06$. The "ribbon" structure, which is due to the presence of the travelling wave can be clearly seen as dark bands in each plot. Within the "ribbon" structure, some near-wall streaks are still visible. In the no-control case, those near-wall streaks are aligned in the streamwise direction, while they are tilted under the modulation of the applied Lorentz force (as shown by the green sinusoidal curves in Fig. 3). Such a phenomenon has also been observed by Pang and Choi (2004) for the spanwise oscillating Lorentz force and by Huang et al. (2010) for the streamwise travelling wave. The tilting effect on the near-wall streaks is the

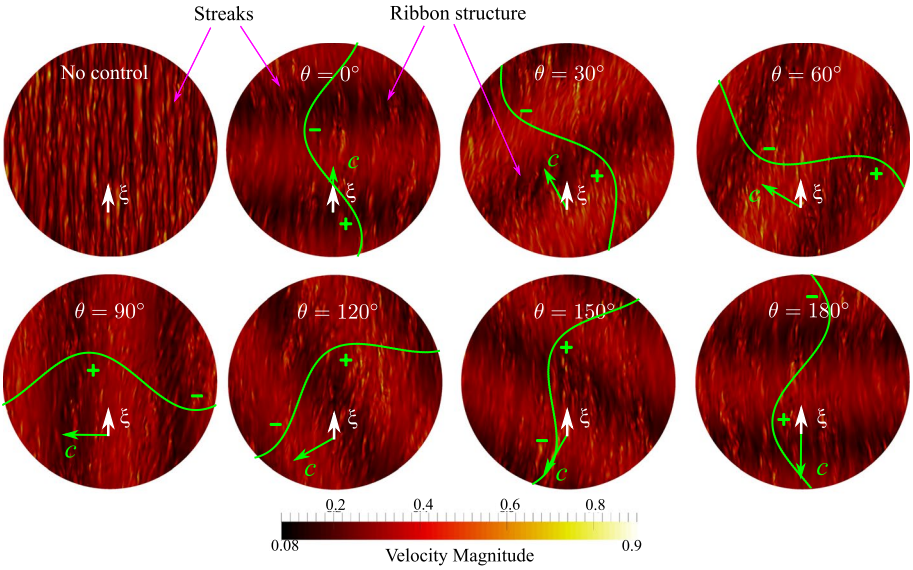

Fig. 3 Instantaneous velocity magnitude $\sqrt{u^2+v^2+w^2}$ at $y^+ \approx 5$ for different travelling wave angles. In each snapshot, the white short arrow indicates the mean flow direction ξ, and the green long arrow indicates the wave travelling direction (with the wave speed c). The green sinusoidal curve shows the instantaneous Lorentz force distribution in the plane, with positive region indicated by +, and negative region indicated by −. The view size is $16h$ in diameter

strongest at $\theta = 0°$ and 180°, while it is hardly visible at $\theta = 90°$, except within the two dark bands. It is also interesting to notice that there is a strong phase relationship between the two dark bands and the Lorentz force distribution. The streak tilting effect becomes clear when the streaks are located in the interface between positive and negative Lorentz force, whereas in the rest area (light bands), the streaks are less visible. Figure 3 clearly demonstrates the gradual change of the interaction between the "ribbon" structure and the near-wall streaks from $\theta = 0°$ to 180°. The nature of this interaction is similar among all the oblique travelling wave cases, and there is always a tilting effect on the near-wall streaks. In the following sections, we will demonstrate the similarity between three typical travelling wave cases (i.e. FST, SP and BST) and spanwise oscillating Lorentz force case, while this was thought to be fundamentally different in previous studies (see Du et al. 2002).

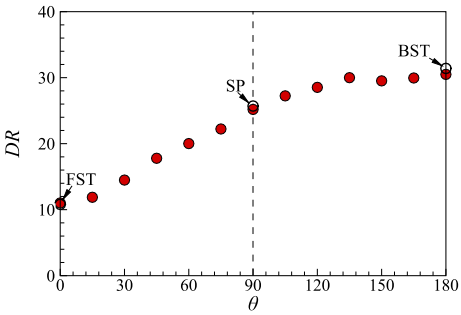

Fig. 4 $\mathcal{DR}$ against travelling wave angle θ for oblique travelling waves. Open circles are data from Table 2 for FST, SP and BST cases

The drag reduction rates obtained for all the 13 oblique travelling wave cases are presented in Fig. 4. The $\mathcal{DR}$ prediction at $\theta = 0°$, 90° and 180° compares well with that of FST, SP and BST. The maximum $\mathcal{DR}$ value is achieved at $\theta = 180°$. However, when $\theta > 90°$, the $\mathcal{DR}$ value is not sensitive to the wave angle θ, and the $\mathcal{DR}$ variation is within the range of $\Delta\mathcal{DR} \approx 3$; while a sharp increase of $\mathcal{DR}$ is observed for $\theta < 90°$, which has $\Delta\mathcal{DR} \approx 15$.

The turbulent statistics are sampled in both x and z directions, and a coordinate transformation is used to transform the turbulent statistics into the streamwise and spanwise directions of the flow. The relationship between statistic variables in the transformed coordinate system (ξ, η, ζ) and the original coordinate system (x, y, z) for the instantaneous and fluctuating streamwise velocities, and the streamwise turbulent shear stress is as below,

$$\begin{aligned} u_\xi &= u\cos\theta - w\sin\theta, \\ \overline{u_\xi'^2} &= (\overline{u^2} - U^2)\cos^2\theta + (\overline{w^2} - W^2)\sin^2\theta - (\overline{uw} - UW)\sin(2\theta), \\ \overline{u_\xi' u_\eta'} &= \overline{uv}\cos\theta - \overline{vw}\sin\theta. \end{aligned} \tag{6}$$

Wall-normal variations of the transformed velocity r.m.s. (root-mean-squared) $u^+_{\xi,rms}, u^+_{\eta,rms}, u^+_{\zeta,rms}$ and the weighted streamwise turbulent shear stress $-(1-y)\overline{u_\xi' u_\eta'}$ are shown in Fig. 5. For all the 13 cases, the wall-normal velocity fluctuation $u^+_{\eta,rms}$ and the spanwise velocity fluctuation $u^+_{\zeta,rms}$ show a monotonic decrease as the wave angle θ is increased. However, the streamwise velocity fluctuation $u^+_{\xi,rms}$ shows an interesting

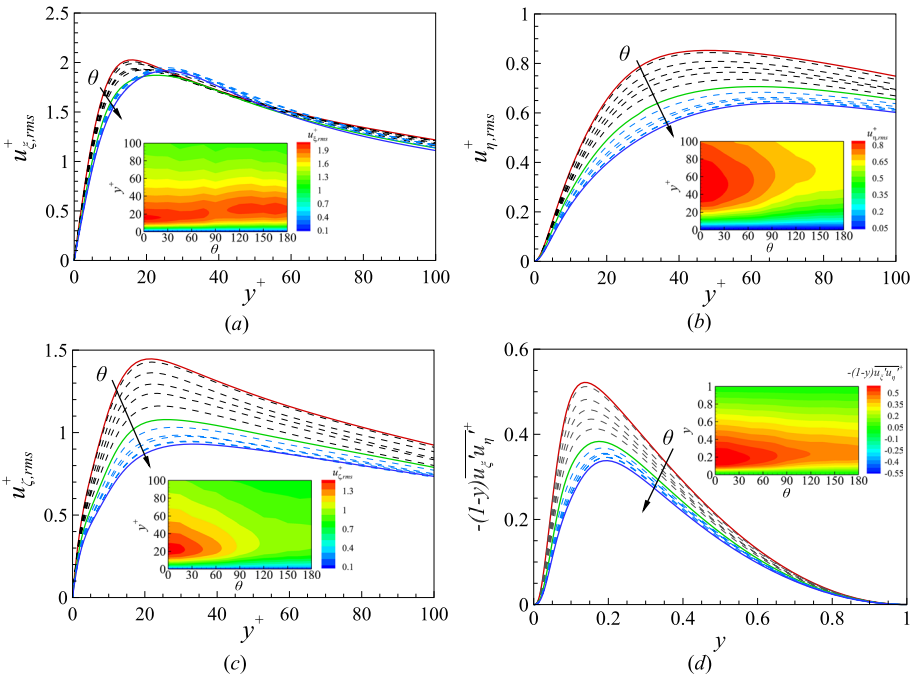

Fig. 5 Turbulent statistics in the transformed coordinate for **a** $u^+_{\xi,rms}$, **b** $u^+_{\eta,rms}$, **c** $u^+_{\zeta,rms}$, and **d** $-(1-y)\overline{u_\xi' u_\eta'}$. The three solid lines (*red*, *green* and *blue*) represent $\theta = 0°$, 90° and 180°, respectively. The inserted contour plots are the corresponding statistics variation in the 2D form

phenomenon at the peak location: when θ increases from 0° to 90°, the peak slightly moves away from the wall, but the strength is weakened; when θ increases from 90° to 180°, the peak keeps moving away from the wall, but the strength is only slightly increased. Such a behaviour of the velocity r.m.s. peak is closely linked to the near-wall streaks and quasi-streamwise vortices. Some evidence can be seen from the snapshots in Fig. 3, but more analyses will be performed in Sect. 3.4. The weighted turbulent shear stress $-(1-y)\overline{u'_\xi u'_\eta}$ indicates the contribution to the skin friction from the turbulent fluctuation according to the F.I.K. identity (Fukagata et al. 2002), and it presents a monotonic decrease, in good agreement with the $\mathcal{DR}$ variation in Fig. 4. Again, a large variation of $-(1-y)\overline{u'_\xi u'_\eta}$ appears for $\theta < 90°$, while a small change for $\theta > 90°$.

3.2 Streamwise and Spanwise Travelling Waves

The drag reduction maps for both streamwise and spanwise travelling waves as a function of the oscillation frequency ω^+ and the wavenumber κ^+ are shown in Fig. 6 for $A = 0.5$ and $\Delta^+ = 10$. The horizontal axis is the oscillation frequency ω^+ (or period T^+), and the vertical axis is the wavenumber κ^+ (or wavelength λ^+). A total of 113 simulations have been performed to construct the two $\mathcal{DR}$ maps. The $\mathcal{DR}$ map for streamwise travelling waves (Fig. 6a) shows a great resemblance to the streamwise travelling wave of spanwise wall velocity (Fig. 6c; see also Fig. 3 in Hurst et al. (2014) and Fig. 2 in Quadrio et al. (2009)), i.e. a drag increase ($\mathcal{DI}$) region (light colour) accompanied by two drag reduction ($\mathcal{DR}$) regions (dark colour) on each side. The $\mathcal{DI}$ region appears when the wave travels at a speed similar to the convection velocity $\mathscr{U}_c^+$ of the near-wall structure, which is typically $\mathscr{U}_c^+ \approx 10$ (Kim and Hussain 1993). However, several differences in the $\mathcal{DR}$ map of streamwise travelling waves between the spanwise Lorentz force and the spanwise wall motion can be observed. Firstly, the $\mathcal{DI}$ region due to the spanwise wall motion has a wave speed $c^+(\equiv \omega^+/\kappa_x^+) \approx 10$, while it is $c^+ \approx 8$ for the spanwise Lorentz force case. Secondly, the $\mathcal{DI}$ region is broader in the present case, which means that the control by spanwise Lorentz force is less effective than that by spanwise wall motion. Thirdly, the maximum drag reduction occurs in the backward streamwise travelling wave case with $\mathcal{DR} = 31$ at $(\omega^+, \kappa_x^+) = (-0.06, 0.002)$, but in the spanwise wall motion case, the optimal $\mathcal{DR}$ case is within the forward travelling wave region with $\mathcal{DR} = 48$ at $(\omega^+, \kappa_x^+) = (0.02, 0.008)$. The backward streamwise travelling wave does not only purely present a drag reduction region, but also a $\mathcal{DI}$ region for large ω^+ and κ_x^+ values (top-left corner of the $\mathcal{DR}$ map).

Figure 6b shows the $\mathcal{DR}$ map for spanwise travelling waves of spanwise Lorentz force. It also presents a $\mathcal{DR}$ region and a $\mathcal{DI}$ region. However, the contour pattern is very different from the $\mathcal{DR}$ map for the streamwise travelling waves (Fig. 6a). The $\mathcal{DR}$ region and the $\mathcal{DI}$ regions are almost vertically separated, which suggests the big similarity between the spanwise travelling wave and the spanwise oscillation of Lorentz force. All the spanwise stationary wave cases ($\omega^+ = 0$) show a drag increase, which varies from $\mathcal{DR} \approx -59$ at $\kappa_z^+ = 0.0026$ to $\mathcal{DR} \approx -146$ at $\kappa_z^+ = 0.0628$. And these drag increase values are much larger than that in the streamwise travelling wave cases, which shows the largest drag increase at $\kappa_x^+ = 0.002$, coresponding to $\mathcal{DR} \approx -17$. A larger drag reduction is associated with a smaller spanwise wavenumber κ_z^+, and this is consistent with the finding by Du et al. (2002). As also pointed out by Xie and Quadrio (2013), the spanwise oscillation case leads to the largest drag reduction comparing to all the spanwise travelling wave cases at the same oscillation frequency.

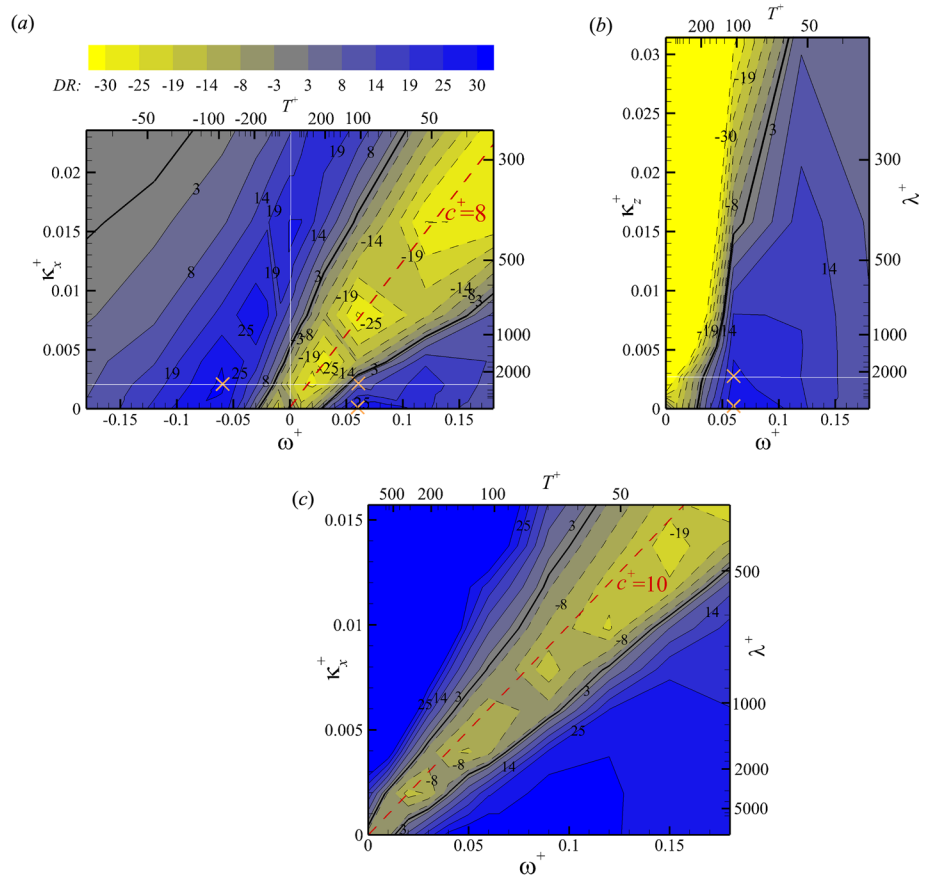

Fig. 6 Drag reduction maps for travelling waves: **a** streamwise travelling waves of Lorentz force, **b** spanwise travelling waves of Lorentz force, and **c** streamwise travelling waves of spanwise wall velocity (data taken from Hurst et al. (2014)). The zero contour level is indicated by black bold lines. Cross symbols mark the OC, FST, SP and BST cases listed in Table 2, and white lines indicate travelling and stationary waves investigated in Fig. 7

Quadrio et al. (2009) proposed a time scale $\mathscr{T}^+$ to link the streamwise travelling wave of spanwise wall velocity with the spanwise wall oscillation. Here, we extend this time scale $\mathscr{T}^+$ to a more general form with the consideration of the travelling wave angle θ. The definition of $\mathscr{T}^+$ is given as below,

$$\mathscr{T}^+ = \frac{\lambda^+}{|\mathscr{U}_c^+ \cos\theta - c^+|}. \tag{7}$$

When $\theta = 0$, it recovers the formula given by Quadrio et al. (2009). Based on $\mathscr{T}^+$, an effective spanwise oscillation frequency $\omega_{eff}^+ = 2\pi/\mathscr{T}^+$ can be defined. The effective oscillation frequencies ω_{eff}^+ for the forward streamwise travelling wave, spanwise travelling wave, backward streamwise travelling wave at $\kappa^+ \approx 0.002$ (as shown by the white solid lines in Fig. 6), and all the 13 oblique travelling wave cases are converted using equation 7 with $\mathscr{U}_c^+ = 8$, and compared in Fig. 7 to the spanwsie oscillating Lorentz force case. Between

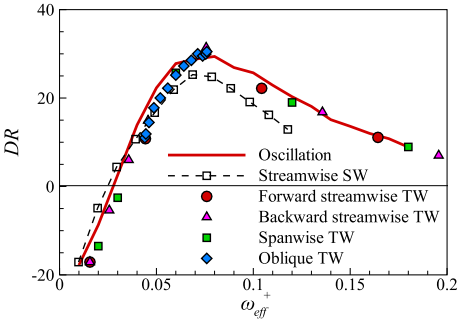

Fig. 7 $\mathcal{DR}$ comparison against the effective oscillation frequency converted using equation 7. $\mathscr{U}_c^+ = 5$ is used for the streamwise stationary wave (SW) ($\omega^+ = 0$), and $\mathscr{U}_c^+ = 8$ for all the others. The streamwise stationary wave (SW), forward/backward streamwise travelling wave (TW) at $\kappa_x^+ = 0.002$ and spanwise travelling wave (TW) at $\kappa_z^+ = 0.0026$ are indicated by the white lines in Fig. 6, and data for the oblique travelling wave (TW) at $\kappa^+ = 0.002$ are taken from Fig. 4

$\omega^+_{eff} = 0.01 \sim 0.2$, all the data points nicely follow the spanwise oscillating Lorentz force case. However, for the streamwise stationary wave, a better comparison in the effective oscillation frequency is achieved with $\mathscr{U}_c^+ = 5$. Here different $\mathscr{U}_c^+$ values are used for better scaling, as the convection velocity of the near-wall turbulent structures varies in both scale and wall-normal height (Jeon et al. 1999; del Álamo and Jiménez 2009), and the Lorentz force generated Stokes layer shifts the near-wall structures along the wall-normal direction. Other data points in the two $\mathcal{DR}$ maps are also converted for comparison (not shown), and it is found that the time scale $\mathscr{T}^+$ does not work well for cases of large wavenumbers. This is also suggested by the large $\mathcal{DR}$ difference at $\omega^+_{eff} > 0.07$ between the streamwise stationary wave case and the spanwise oscillation case. With the focus on the trend of $\mathcal{DR}$ change against ω^+_{eff}, Fig. 7 suggests that all the travelling wave cases at $\kappa^+ \approx 0.002$ can be analogue to the spanwise oscillation case with the consideration of the wave speed and wave angle. The good agreement between the converted oblique travelling waves and the spanwise oscillation strongly supports that the interaction between the "ribbon" structure and the near-wall streaks is similar to the situation of spanwise oscillation, although the former streaks vary the spanwise tilting direction in space, while the latter streaks vary in time. In the following sections, this similarity reflected in the turbulent statistics and structure dynamics will be further explored.

3.3 Statistics and Spectra

The governing equation of the quiescent laminar flow under spanwise oscillating Lorentz force is given as below (Berger et al. 2000),

$$\begin{aligned} &\frac{\partial w}{\partial t} = \frac{\partial^2 w}{\partial y^2} + Ae^{-y/\Delta}\sin(-\omega t), \\ &\text{B.C.}: w = 0|_{y=0}, \end{aligned} \tag{8}$$

which has the following analytical solution,

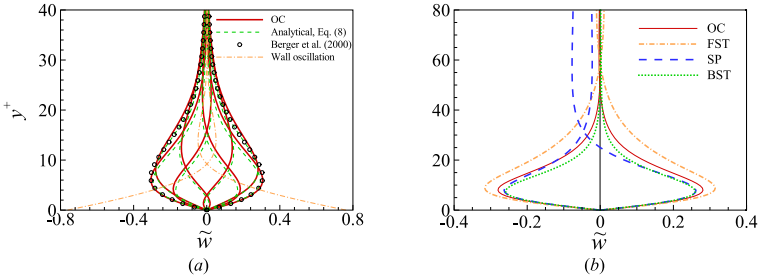

Fig. 8 Spanwise mean velocity profiles for **a** OC compared with the analytical solution and the spanwise wall oscillation at $\omega^+ = 0.06$ (*orange dash-dot lines*), and **b** travelling wave cases at two given phases, i.e. $\phi = 0$ and π

$$w = \widehat{A}e^{-\widetilde{y}}[\omega\cos(\omega t) + c\sin(\omega t)] - \widehat{A}e^{-\widehat{y}}\left[\omega\cos(\omega t - \widehat{y}) + c\sin(\omega t - \widehat{y})\right], \tag{9}$$

where $\widehat{A} = \frac{A}{c^2+\omega^2}$, $c = \frac{1}{\Delta^2}$, $\widehat{y} = y\sqrt{\frac{\omega}{2}}$, $\widetilde{y} = \frac{y}{\Delta}$. The analytical solutions at 8 phases of one oscillation period are shown in Fig. 8a together with the turbulent spanwise mean velocity profiles at the same oscillation frequency. The envelope of the laminar solution has also been given by Berger et al. (2000). As can be seen, the laminar and turbulent profiles are similar to each other close to the wall, while they deviate from each other further away from the wall. Due to the no-slip wall boundary condition, the maximum spanwise mean velocity appears within $0 < y^+ < \Delta^+$. This gives an obvious difference of the spanwise mean velocity profiles between the OC case and the spanwise wall oscillation case (Hurst et al. 2014). For FST, SP and BST cases, the spanwise mean velocity profiles vary in both time and space, and they are compared to the OC case in Fig. 8b, with the profiles shown at only two phases, i.e. $\phi = 0$ and π. These two phases are chosen to roughly outline the envelope of the spanwise mean velocity profiles for each case. Again, within the viscous sublayer ($y^+ < 5$), the spanwise mean velocity profiles are very similar. However, the decay rates of the spanwise mean velocity among those four cases are different further away from the wall. For SP, the Lorentz force travels in the positive spanwise direction, thus it induces positive net mass flow in the spanwise direction near the wall and negative spanwise mass flow further away from the wall ($\tilde{w} = -0.05$ at the core region), as also observed by Xie and Quadrio (2013). The LGSL thickness δ^+ can be defined as the wall-normal distance

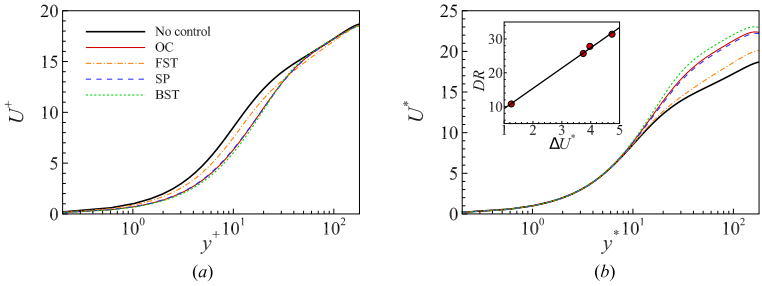

Fig. 9 Streamwise mean velocity profile compared among the no-control, OC, FST, SP and BST cases scaled in viscous units of **a** the no-control reference case, and **b** each controlled case. The inserted plot shows the linear scaling of $\mathcal{DR}$ against the streamwise mean velocity shift in the logarithmic region

where the spanwise mean velocity decreases to e^{-1} of the maximum value (Quadrio et al. 2009). This gives $\delta^+ = 20$, 25 and 18 for OC, FST and BST, respectively. We will show later that this Stokes layer plays a role of displacing the turbulence structure in the near-wall region.

The streamwise mean velocity profiles for OC, FST, SP and BST are compared in Fig. 9 with the no-control case. Two inner scaling are considered, one is scaled by the viscous units of the no-control reference case (Fig. 9a), and the other is scaled by the viscous units of each controlled case (Fig. 9b). With the same inner units used for all the cases, the profiles are equivalent to those scaled in the outer units. Indeed, we can see from Fig. 9a that the outer regions of the streamwise mean velocity profiles are overlaid with each other well, indicating that the Lorentz force generated Stokes layer only affects the flow in the near-wall region. Due to the drag reduction of all the presented cases, the near-wall gradients of the streamwise velocity are all decreased. However, when the streamwise mean velocity profile is scaled with the inner units of each case, a comment feature of the near-wall drag reduction control appears, such as in the texture surface (Garcia-Mayoral et al. 2019), spanwise wall oscillation (Hurst et al. 2014; Gatti and Quadrio 2016), opposition control (Ibrahim et al. 2021), in which the viscous layers are perfectly collapsed for all the cases, while a upward shift of the streamwise mean velocity profile is present in the logarithmic region, indicating the thickening of the viscous layer of the controlled flow. The upward shift of the profile is $\Delta U^* = 4.0$, 1.3, 3.7 and 4.7 for the controlled cases OC, FST, SP and BST, respectively, in comparison with the no-control reference case. This gives a very good linear correlation between ΔU^* and the $\mathcal{DR}$ value, i.e. $\mathcal{DR} = 6.0\Delta U^* + 3.4$, as indicated by the black solid line in the inserted plot of Fig. 9b.

The turbulent velocity and vorticity fluctuations for OC, FST, SP and BST are shown in Fig. 10. For the three travelling wave cases, the behaviour of $u^+_{i,rms}$ is the same as that in the oblique travelling wave shown in Fig. 5. The statistics modulation over the entire wall-normal distance for the travelling wave cases is similar to the oscillation case. As can be seen, over the entire channel height, u^+_{rms} decreases for all the four drag reduction cases,

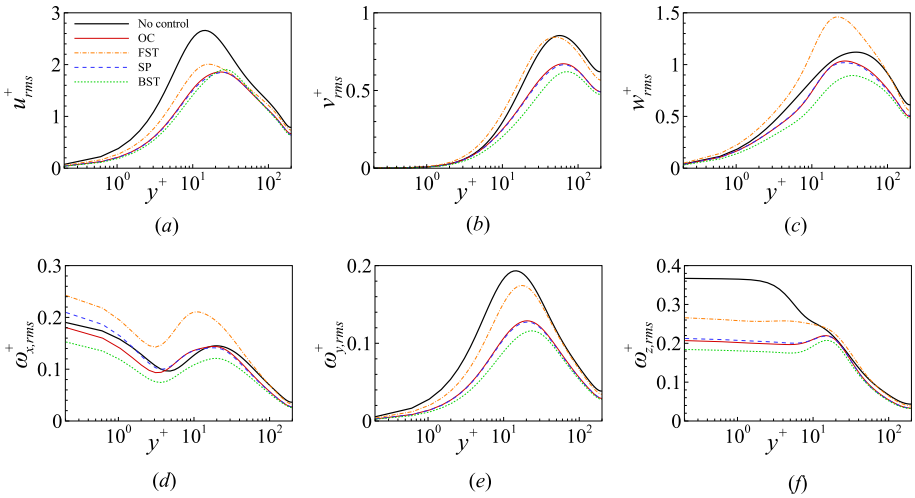

Fig. 10 R.m.s. of the velocity and vorticity fluctuations compared among the no-control, OC, FST, SP and BST cases for **a** u^+_{rms}, **b** v^+_{rms}, **c** w^+_{rms}, **d** $\omega^+_{x,rms}$, **e** $\omega^+_{y,rms}$, and **f** $\omega^+_{z,rms}$

especially for the near-wall peak, which has a maximum decrease of around 30% for OC. The near-wall peak of u^+_{rms} appears at $y^+ \approx 14$ for the no-control case (Kim et al. 1987), while it moves to $y^+ = 16$, 20, 24 and 28 for OC, FST, SP and BST, respectively. The peak of v^+_{rms} monotonically decreases. The peak value modulation on w^+_{rms} is very different for FST, where 30% increase in the w^+_{rms} peak value is observed despite that FST gives around 11% drag reduction. For the vorticity plots, $\omega^+_{y,rms}$ is normally used to measure the strength of the near-wall streaks (Le et al. 2000). As can be see, $\omega^+_{y,rms}$ decreases for all the controlled cases (Fig. 10e), which is similar to v^+_{rms} plot. Surprisingly, $\omega^+_{x,rms}$ does not decrease for all cases (Fig. 10d). For example, $\omega^+_{x,rms}$ increases in the region of $4 < y^+ < 14$ for OC and SP, while $\omega^+_{x,rms}$ increases within the whole channel height for FST. This is reminiscent of the drag reduction mechanism proposed by Du et al. (2002) that an appropriate enhancement of the streamwise vortices can lead to the weakening of the streak intensity. Considering that all the four controlled cases present drag reduction (for the exact $\mathcal{DR}$ values see Table 2), the $\mathcal{DR}$ value correlates better with the wall-normal vorticity, $\omega^+_{y,rms}$, as having been found by Chung and Talha (2011) for the near-wall opposition control. Based on the change of the velocity and vorticity fluctuation statistics, the spanwise travelling wave case is very similar to the spanwise oscillation case.

The energy change in the streamwise velocity fluctuation is checked by the two-dimensional pre-multiplied streamwise velocity spectra $k_x k_z E_{uu}$ at $y^+ \approx 10$, as shown in Fig. 11. At this location, the near-wall streaks in the no-control case are indicated by an energy peak site associated with the length scale $(\lambda^+_x, \lambda^+_z) \approx (1000, 100)$. When the flow is controlled by spanwise Lorentz force, there is a significant reduction in the streamwise length scale of the near-wall streaks, with $\lambda^+_x \approx 350$ for OC and SP, $\lambda^+_x \approx 200$ for FST, and $\lambda^+_x \approx 400$ for BST, as indicated by the arrows in the streamwise pre-multiplied spectra. The data suggests that the near-wall streaks are broken-up by the travelling waves, resulting in a significant amount of energy reduction in the large scales $\lambda^+_x > 1000$, which is also evidenced from the instantaneous streaks plot in Fig. 3. The length scale change in the spanwise direction is not obvious, i.e. $\lambda^+_z \approx 104$, 109, 104 and 109 for the OC, FST, SP and BST cases, as indicated by the arrows in the spanwise pre-multiplied spectra. However, the peak location in the spanwise spectra is too broad for the controlled cases, which makes it difficult to draw

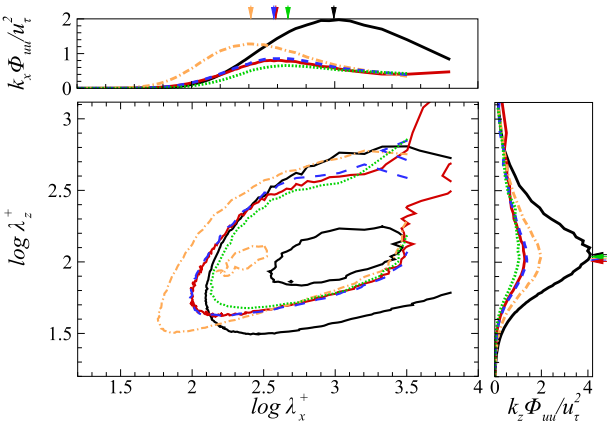

Fig. 11 Two- and one-dimensional pre-multiplied streamwise velocity spectra at $y^+ \approx 10$ for the no-control case (*black solid line*) and the controlled cases (see Table 2 for the line keys). 7% and 60% contour lines of the no-control case peak value are shown in the two-dimensional plot for each spectrum

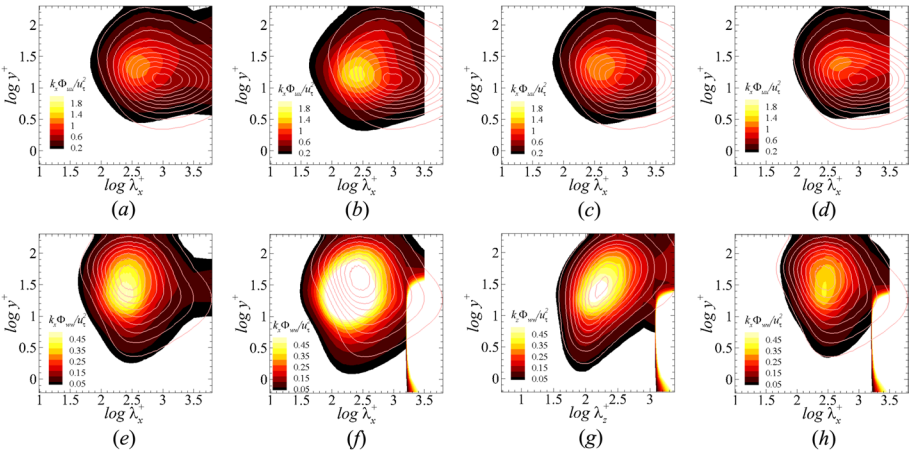

Fig. 12 One-dimensional pre-multiplied spectra over the half channel height for **a**, **e** OC, **b**, **f** FST, **c**, **g** SP, and **d**, **h** BST. The no-control case is shown by contour lines, while the controlled cases are shown by shaded contours. **a**, **b**, **c**, **d** are the spectra of k_xE_{uu}, **e**, **f**, **h** the spectra of k_xE_{ww}, and **g** the spectrum of k_zE_{ww}

a solid conclusion about the peak movement. But it is clear from the spanwise spectra plot that the portion of energy distributed among the large scales ($\lambda_z^+ > 100$) becomes larger in the controlled cases compared to the no-control one.

The one-dimensional pre-multiplied spectra for the streamwise velocity over the channel are shown in Figs. 12**a**–**d** for OC, FST, SP and BST, with comparison to the no-control case. It is clear to track the wall-normal location of the streamwise velocity spectra peak, which indicates the near-wall streaks location, for all four travelling wave cases. Again, this energetic peak site moves further away from the wall for all the controlled cases, consistent with the u_{rms}^+ plot in Fig. 10a. Figs. 12e–h show the same spectra for the spanwise velocity. To emphasise the energy in the Lorentz force generated Stokes layer (LGSL), k_zE_{ww} is shown for SP, while k_xE_{ww} is shown for the other controlled cases. The energy contained in the LGSL as shown in Fig. 12f–h has the scale of the domain size and keeps energetic in the whole LGSL. For OC, there is no such an energetic site due to the force homogeneity in space. A complicated interaction exist between the LGSL and the most energetic spanwise velocity structure, which has the length scale of $(\lambda_x^+, \lambda_z^+) \approx (300, 200)$, corresponding to the near-wall quasi-streamwise vortices (Hwang 2015). The LGSL does not obviously modulate the scale of the near-wall quasi-streamwise vortices, but mainly changes the containing energy. This modification seems to be closely related to the thickness of the LGSL. For FST, the thickness of LGSL is the largest, and the near-wall quasi-streamwise vortices are amplified, while for OC, SP and BST, the near-wall quasi-streamwise vortices are weakened. This observation is also consistent with the w_{rms}^+ profile variation in Fig. 10c.

3.4 Structure Dynamics

To study the applied Lorentz force effect on the near-wall quasi-streamwise vortices, the ensemble averaged λ_2 structures are analysed, following the eduction scheme proposed by Jeong et al. (1997). The ensemble averaged positive (clockwise rotating, $\omega_x' > 0$) λ_2 structure is shown in Fig. 13a for the no-control case. Agreeing with Jeong et al. (1997), the λ_2 structure sits at a wall distance of $y^+ \approx 20$, with a tilting angle of $-5°$ and an inclination

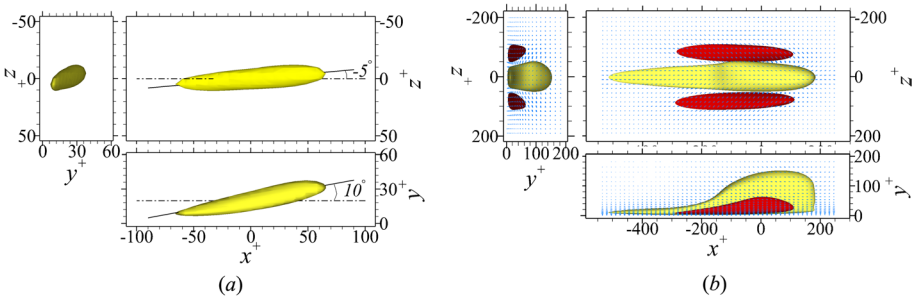

Fig. 13 **a** Ensemble averaged positive λ_2 (clockwise rotating, $\omega_x' > 0$) structure, visualised by $\lambda_2^+ = -0.005$; **b** the characteristic eddy, visualised by $u' = 0.35$ (*yellow*) and $u' = -0.35$ (*red*), with arrows indicating the fluctuating velocity vector. These structures are for the no-control case, and the flow goes from left to right

angle of 10°. Moreover, the proper orthogonal decomposition (POD) is used to capture the characteristic eddy in the turbulent flow (Moin and Moser 1989), which is also the representative of the near-wall streaks. The characteristic eddy for the high-speed streak is shown in Fig. 13b for the no-control case. The visualised high-speed streak is $\lambda_x^+ \approx 700$ in length based on the iso-surface threshold used for the visualisation, and this is close to the inner energy site in the pre-multiplied spectrum for the streamwise velocity fluctuation (Fig. 11). Beside the high-speed streak are two low-speed streaks. The spanwise spacing between two low-speed streaks is $\lambda_z^+ \approx 100$. As the quasi-streamwise vortices and streaks form the near-wall self-sustaining cycle and are responsible for the skin friction generation, their dynamics modulation in the presence of the Lorentz force generated Stokes layer is crucial for the understanding of the drag reduction mechanism.

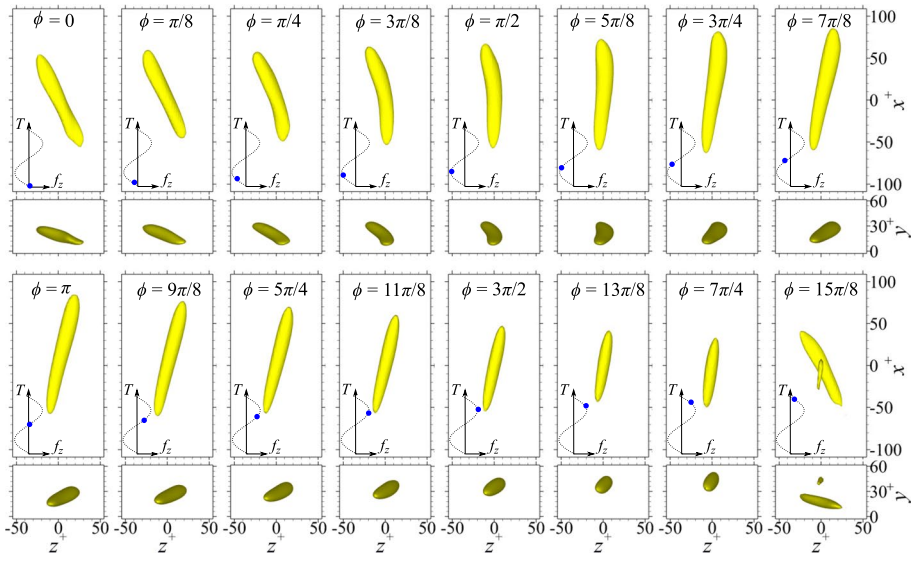

Fig. 14 Conditional averaged positive λ_2 structure at 16 equally separated phases of one oscillation period for OC. The structures are visualised by $\lambda_2^+ = -0.01$

The ensemble averaged λ_2 structure analysis is extended to study the spanwise oscillating Lorentz force case (OC). Similar analysis has been performed for the spanwise wall oscillation control (Hurst 2013; Yakeno et al. 2014). The simulation of OC is run for 10 oscillation periods after the transient process, with the three-dimensional field data stored at 16 equally separated phases within each period, and the ensemble average process is then applied at each phase. The conditional averaged positive λ_2 structures at 16 phases are shown in Fig. 14. Generally, the positive structure changes the spanwise tilting angle periodically in the $x-z$ plane, and the centre position moves away from the wall. At the beginning of the oscillation period, the positive structure is negatively tilted in the $x-z$ plane, and it is closest to the wall. As the spanwise Lorentz force goes towards the negative spanwise direction (left), the positive structure starts to turn in clockwise direction in the $x-z$ plane until the tilting angle is positive at the end of the oscillation period. Meanwhile, the positive structure keeps moving away from the wall, and its strength increases in the first half period then decreases in the second half. Due to the symmetry of the flow, the negative structure shows a similar behaviour, but with half a period shift in phase compared to its positive counterpart. It is noticed that, at $\phi = 15\pi/8$, two positive structures are identified, i.e. one weak structure further away from the wall, and one strong structure close to the wall. This closes the cycle of the near-wall quasi-streamwise vortex structure dynamics under spanwise oscillating Lorentz force, and it is similar to what observed in the boundary layer of spanwise wall oscillation (Hurst 2013; Yakeno et al. 2014).

The quasi-streamwise vortices directly induce high- and low-speed streaks as a companion (Jeong et al. 1997). Fig. 15 shows the streak behaviour for OC at 16 equally separately phases during one oscillation period. The high-speed streak is $\lambda_x^+ \approx 500$ in length (not shown), much shorter than that in the no-control case (Fig. 13b), which indicates that the near-wall streaks are significantly weakened (Moarref and Jovanović 2012). Recalling the thickness of LGSL is $\delta^+ = 20$ for OC (Fig. 8b), a clear evidence shows that both the high- and low-speed streaks are significantly tilted inside and above the Stokes layer, up to $y^+ \approx 60$, which corresponds to the streak angle tilting in the spanwise

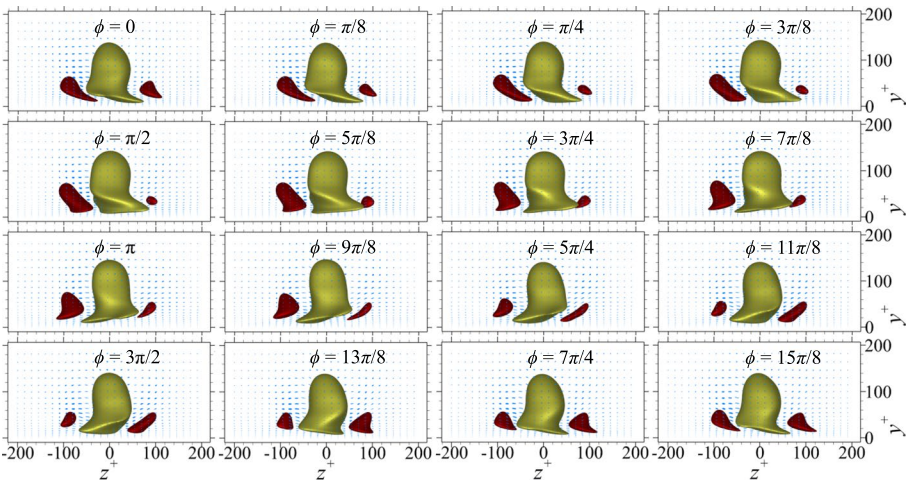

Fig. 15 Tail view of the characteristic eddy at 16 equally separated phases during one oscillation period for the OC case. The high- and low-speed streaks are visualised by $u' = \pm 0.35$, respectively

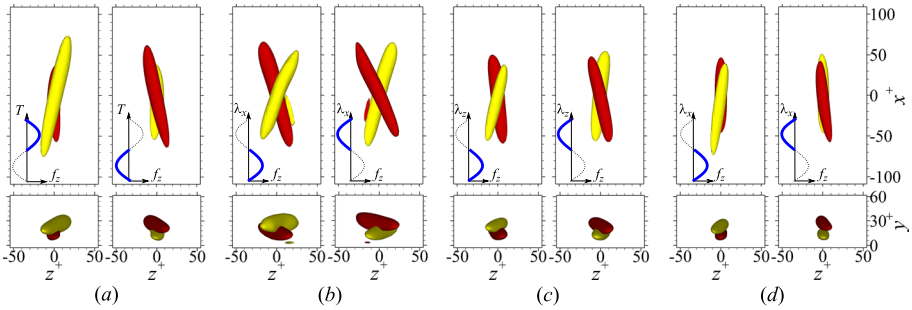

Fig. 16 Conditional averaged positive (*yellow*) and negative (*red*) λ_2 structures in the positive (*left panel*) and negative (*right panel*) Lorentz force regions for **a** OC, **b** FST, **c** SP and **d** BST. The structures are visualised by $\lambda_2^+ = -0.01$

direction, as also observed for the tilting of the quasi-streamwise vortices shown in Fig. 14. We further checked that the structure tilting angle can roughly match the shear angle at $y^+ \approx 10$, similar to the situation in spanwise wall oscillation control (Touber and Leschziner 2012; Yakeno et al. 2014). It is noted that the overall dynamic variation of the near-wall vortices and streaks has recently been computed with the exact coherent state in plane Couette flow under spanwise wall oscillation (Bengana et al. 2022), and there is a qualitative agreement between the captured structure dynamics.

To verify the vortex structure behaviour for FST, SP and BST, the positive and negative λ_2 structures are conditioned in the positive and negative Lorentz force regions, separately. As can be seen from the instantaneous flow fields shown in Fig. 3, the near-wall streaks are modulated differently in these two regions. The conditioned λ_2 structures are shown in Fig. 16. Since one wavelength is only divided into two parts, the resolution is lower than the conditioned structures for OC, which can be averaged at any precise phase. To make the comparison more straightforward, the λ_2 structures are also conditioned in the positive ($\phi = \pi \sim 15\pi/8$) and negative ($\phi = 0 \sim 7\pi/8$) Lorentz force regions only for OC, as shown in Fig. 16a. The structure behaviours in the positive and negative Lorentz force regions for the travelling wave cases strongly resemble those of OC. The positive and negative structures reside in two very different wall-normal locations, i.e. the upper structure is at $y^+ \approx 25$, while the lower structure is at $y^+ \approx 14$ (u^+_{rms} peak location in the no-control case, Fig. 10a). In the positive force region, the negative λ_2 structure is lower and the positive λ_2 structure is higher; while the opposite situation occurs in the negative force region. The result suggests that the positive or negative Lorentz force only favours one type of the near-wall quasi-streamwise vortices, as in other three-dimensional turbulent boundary layers (e.g. Holstad et al. 2012).

When visualised with the same λ_2 criteria, differences in the structure strength, tilting angle can be observed among OC, FST, SP and BST, as shown in Fig. 17. The tilting angles of both the upper and lower structures correlate well with the $\mathcal{DR}$ values, which shows a slope of -0.67. The overall tilting angle of the upper structure is always larger than that of the lower one for the controlled cases, since the lower structure has both positive and negative tilting angle variations, but the upper one is more stationary (Fig. 14). When the strength is measured by the maxima of the $-\lambda_2$ field, the upper structure is always weaker than the lower one, which is consistent with the continuous structure dynamics in the spanwise oscillating LGSL shown in Fig. 14. The strength variation of the upper structure is

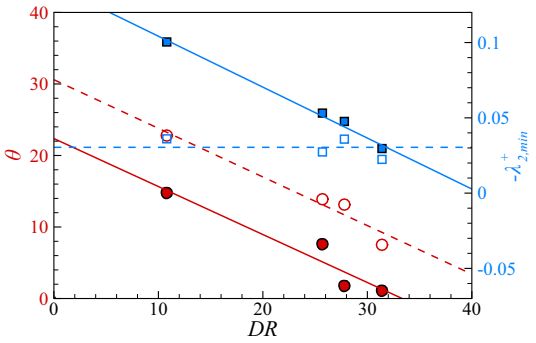

Fig. 17 Correlation of $\mathcal{DR}$ with the structure tilting angle (*circles*) and the structure strength (*squares*) for the upper (*open symbols*) and lower (*closed symbols*) structures

negligible among all the four controlled cases, but a big strength variation is observed for the lower structure, and this strength variation also presents a good correlation with the $\mathcal{DR}$ value. The results suggest that the strong link between the drag reduction and the near-wall streaks and quasi-streamwise vortices modulation by various travelling waves.

4 Conclusions

A systematic study of the streamwise, spanwise and oblique travelling waves by spanwise Lorentz force has been conducted in the present study, with a maxima of about 30% drag reduction achieved at the explored Lorentz force strength $A = 0.5$ and penetration depth $\Delta^+ = 10$. The overall drag reduction maps in the $\omega^+ - \kappa_x^+$ and $\omega^+ - \kappa_z^+$ space have been constructed with a large amount of DNS data for both streamwise and spanwise travelling waves. Depending on the control parameters, the travelling wave of Lorentz force can effectively achieve drag reduction, especially at relatively large wavelengths. When the wave travels at $c^+ \approx 8$ along the downstream direction or remains stationary in the spanwise direction, the Lorentz force can instead amplify the turbulent structures and lead to a corridor of $\mathcal{DI}$ region. Particularly, the travelling wave at $(\kappa^+, c^+) = (0.002, 30)$ was designed to align the mean flow with an angle to the x direction, and the effect of the travelling wave angle at a fixed wavelength was quantified for the first time thanks to a careful experiment design. The most effective drag reduction case of the oblique travelling wave under the studied control parameters was found to be the one which travels backward in the streamwise direction, i.e. $\theta = 180°$. The interaction between the travelling wave generated "ribbon" structure and the near-wall streaks is not just a phenomenon in the spanwise travelling wave case as originally observed by Du et al. (2002), but also a common feature shared by all travelling wave cases of Lorentz force. Detailed structure dynamics analyses suggest that for $\mathcal{DR}$ cases, the spanwise Lorentz force creates an asymmetry between the positive and negative near-wall quasi-streamwise vortices, and interrupts the formation of long high- and low-speed streaks, which essentially weakens the self-sustaining process of the turbulent structure and leads to the skin-friction drag reduction. The travelling waves and the spanwise oscillation of Lorentz force share many similarities in the turbulent statistics and energy spectra. The $\mathcal{DR}$ values of the travelling wave cases were found to coorelate well with the spanwise oscillating Lorentz force case via the time scale $\mathcal{T}^+ = \lambda^+/(\mathcal{U}_c^+ \cos\theta - c^+)$, at least for the small wavenumber regime investigated in this work.

Acknowledgements The authors would like to thank EPSRC for the computational time made available on the UK supercomputing facility ARCHER/ARCHER2 via the UK Turbulence Consortium (EP/R029326/1). The authors also acknowledge the use of HPC machines at Scientific Computing RTP, University of Warwick. Q.Y. was sponsored by the joint scholarship between University of Warwick and China Scholarship Council. Q.Y. also acknowledges the help from Dr E. Hurst during this project.

Author Contributions QY and YMC wrote the main manuscript text. QY prepared all figures. All authors reviewed the manuscript.

Declarations

Conflict of interest The authors declare that they have no conflict of interest.

References

Albers, M., Meysonnat, P.S., Fernex, D., et al.: Drag reduction and energy saving by spanwise traveling transversal surface waves for flat plate flow. Flow Turbul. Combust. **105**(1), 125–157 (2020)

Auteri, F., Baron, A., Belan, M., et al.: Experimental assessment of drag reduction by traveling waves in turbulent pipe flow. Phys. Fluids **22**(11), 115103 (2010)

Bengana, Y., Yang, Q., Tu, G., et al.: Exact coherent states in plane Couette flow under spanwise wall oscillation. J. Fluid Mech. **947**, A2 (2022)

Berger, T.W., Kim, J., Lee, C., et al.: Turbulent boundary layer control utilizing the Lorentz force. Phys. Fluids **12**(3), 631–649 (2000)

Bird, J., Santer, M., Morrison, J.F.: Experimental control of turbulent boundary layers with in-plane travelling waves. Flow Turbul. Combust. **100**(4), 1015–1035 (2018)

Breuer, K.S., Park, J., Henoch, C.: Actuation and control of a turbulent channel flow using Lorentz forces. Phys. Fluids **16**(4), 897–907 (2004)

Choi, H., Moin, P.: Effects of the computational time step on numerical solutions of turbulent flow. J. Comput. Phys. **113**(1), 1–4 (1994)

Chung, Y.M., Talha, T.: Effectiveness of active flow control for turbulent skin friction drag reduction. Phys. Fluids **23**(2), 025102 (2011)

Corke, T.C., Thomas, F.O.: Active and passive turbulent boundary-layer drag reduction. AIAA J. **56**(10), 3835–3847 (2018)

Crawford, C.H., Karniadakis, G.E.: Reynolds stress analysis of EMHD-controlled wall turbulence. Part I. Streamwise forcing. Phys. Fluids **9**(3), 788–806 (1997)

de Giovanetti, M., Hwang, Y., Choi, H.: Skin-friction generation by attached eddies in turbulent channel flow. J. Fluid Mech. **808**, 511–538 (2016)

del Álamo, J.C., Jiménez, J.: Estimation of turbulent convection velocities and corrections to Taylor's approximation. J. Fluid Mech. **640**, 5–26 (2009)

Du, Y., Karniadakis, G.E.: Suppressing wall turbulence by means of a transverse traveling wave. Science **288**, 1230–1234 (2000)

Du, Y., Symeonidis, V., Karniadakis, G.E.: Drag reduction in wall-bounded turbulence via a transverse travelling wave. J. Fluid Mech. **457**, 1–34 (2002)

Fukagata, K., Iwamoto, K., Kasagi, N.: Contribution of Reynolds stress distribution to the skin friction in wall-bounded flows. Phys. Fluids **14**(11), L73–L76 (2002)

Garcia-Mayoral, R., Gomez-de Segura, G., Fairhall, C.T.: The control of near-wall turbulence through surface texturing. Fluid Dyn. Res. **51**(011), 410 (2019)

Gatti, D., Quadrio, M.: Reynolds-number dependence of turbulent skin-friction drag reduction induced by spanwise forcing. J. Fluid Mech. **802**, 553–582 (2016)

Hamilton, J.M., Kim, J., Waleffe, F.: Regeneration mechanisms of near-wall turbulence structures. J. Fluid Mech. **287**, 317–348 (1995)
Henoch, C., Stace, J.: Experimental investigation of a salt water turbulent boundary layer modified by an applied streamwise magnetohydrodynamic body force. Phys. Fluids **7**(6), 1371–1383 (1995)
Holstad, A., Andersson, H.I., Pettersen, B.: Turbulence in a skewed three-dimensional wall-bounded shear flow: effect of mean vorticity on structure modification. Int. J. Numer. Meth. Fluids **69**, 1299–1325 (2012)
Huang, L., Fan, B., Dong, G.: Turbulent drag reduction via a transverse wave travelling along streamwise direction induced by Lorentz force. Phys. Fluids **22**(1), 015103 (2010)
Huang, L., Choi, K., Fan, B., et al.: Drag reduction in turbulent channel flow using bidirectional wavy Lorentz force. Sci. China Phys. Mech. Astron. **57**(6), 1–8 (2014)
Huang, L.P., Choi, K.S., Fan, B.C.: Formation of low-speed ribbons in turbulent channel flow subject to a spanwise travelling wave. In: European Turbulence Conference **13**(2011)
Hurst, E.: A numerical study of turbulent drag reduction using streamwise travelling waves of spanwise wall velocity. PhD thesis, University of Warwick (2013)
Hurst, E., Yang, Q., Chung, Y.M.: The effect of Reynolds number on turbulent drag reduction by streamwise travelling waves. J. Fluid Mech. **759**, 28–55 (2014)
Hwang, Y.: Statistical structure of self-sustaining attached eddies in turbulent channel flow. J. Fluid Mech. **767**, 254–289 (2015)
Ibrahim, J.I., Gómez-De-Segura, G., Chung, D., et al.: The smooth-wall-like behaviour of turbulence over drag-altering surfaces: a unifying virtual-origin framework. J. Fluid Mech. **915**, 1–39 (2021)
Jeon, S., Choi, H., Yoo, J.Y., et al.: Space-time characteristics of the wall shear-stress fluctuations in a low-reynolds-number channel flow. Phys. Fluids **11**(10), 3084–3094 (1999)
Jeong, J., Hussain, F., Schoppa, W., et al.: Coherent structures near the wall in a turbulent channel flow. J. Fluid Mech. **332**, 185–214 (1997)
Jiang, D., Zhang, H., Fan, B., et al.: Vortex structures and drag reduction in turbulent channel flow with the effect of space-dependent electromagnetic force. Ocean Eng. **176**, 74–83 (2019)
Jung, W.J., Mangiavacchi, N., Akhavan, R.: Suppression of turbulence in wall-bounded flows by high-frequency spanwise oscillations. Phys. Fluids A **4**(8), 1605–1607 (1992)
Karniadakis, G.E., Choi, K.S.: Mechanisms on transverse motions in turbulent wall flows. Annu. Rev. Fluid Mech. **35**, 45–62 (2003)
Kim, J., Hussain, F.: Propagation velocity of perturbations in turbulent channel flow. Phys. Fluids **5**, 695–706 (1993)
Kim, J., Moin, P., Moser, R.: Turbulence statistics in fully developed channel flow at low Reynolds number. J. Fluid Mech. **177**, 133–166 (1987)
Kravchenko, A.G., Choi, H., Moin, P.: On the relation of near-wall streamwise vortices to wall skin friction in turbulent boundary layers. Phys. Fluids A **5**(12), 3307–3309 (1993)
Le, A.T., Coleman, G.N., Kim, J.: Near-wall turbulence structures in three-dimensional boundary layers. Int. J. Heat Fluid Flow **21**(5), 480–488 (2000)
Lee, J.H., Sung, H.J.: Reponse of a spatially developing turbulent boundary layer to a spanwise oscillating electromagnetic force. J. Turbul. **6**(39), 1–15 (2005)
Leschziner, M., Choi, H., Choi, K.S.: Flow control approaches in aerodynamics: progress and prospects. Philos. Trans. R. Soc. A **369**(1940), 1349–1351 (2011)
Leschziner, M.A.: Friction-drag reduction by transverse wall motion—a review. J. Mech. **36**(5), 649–663 (2020)
Mamori, H., Fukagata, K.: Drag reduction effect by a wave-like wall-normal body force in a turbulent channel flow. Phys. Fluids **26**(11), 115104 (2014)
Marusic, I., Chandran, D., Rouhi, A., et al.: An energy-efficient pathway to turbulent drag reduction. Nat. Commun. **12**(1), 1–8 (2021)
Moarref, R., Jovanović, M.R.: Model-based design of transverse wall oscillations for turbulent drag reduction. J. Fluid Mech. **707**, 205–240 (2012)
Moin, P., Moser, R.D.: Characteristic-eddy decomposition of turbulence in a channel. J. Fluid Mech. **200**, 471–509 (1989)
Pang, J., Choi, K.S.: Turbulent drag reduction by Lorentz force oscillation. Phys. Fluids **16**(5), L35–L38 (2004)
Quadrio, M.: Drag reduction in turbulent boundary layers by in-plane wall motion. Philos. Trans. R. Soc. A **369**, 1428–1442 (2011)
Quadrio, M., Ricco, P., Viotti, C.: Streamwise-travelling waves of spanwise wall velocity for turbulent drag reduction. J. Fluid Mech. **627**, 161–178 (2009)
Ricco, P., Skote, M., Leschziner, M.A.: A review of turbulent skin-friction drag reduction by near-wall transverse forcing. Prog. Aerosp. Sci. **123**(100), 713 (2021)
Talha, T., Chung, Y.M.: Large-eddy simulations of temporally accelerating turbulent channel flow. J. Turbul. **16**(11), 1091–1113 (2015)

Touber, E., Leschziner, M.A.: Near-wall streak modification by spanwise oscillatory wall motion and drag-reduction mechanisms. J. Fluid Mech. **693**, 150–200 (2012)
Viotti, C., Quadrio, M., Luchini, P.: Streamwise oscillation of spanwise velocity at the wall of a channel for turbulent drag reduction. Phys. Fluids **21**(11), 115109 (2009)
Xie, W., Quadrio, M.: Wall turbulence control by spanwise travelling waves. In: European Turbulence Conference **14**(2013)
Yakeno, A., Hasegawa, Y., Kasagi, N.: Modification of quasi-streamwise vortical structure in a drag-reduced turbulent channel flow with spanwise wall oscillation. Phys. Fluids **26**(8), 085109 (2014)
Yang, Q., Willis, A.P., Hwang, Y.: Exact coherent states of attached eddies in channel flow. J. Fluid Mech. **862**, 1029–1059 (2019)
Zhao, M.X., Huang, W.X., Xu, C.X.: Drag reduction in turbulent flow along a cylinder by circumferential oscillating Lorentz force. Phys. Fluids **31**(9), 095104 (2019)